



Investigation on the Fatigue Crack Propagation Behavior of L360MS Pipeline Steel Welded Joints with Inconel 625 Weld Metal

Yunfeng Hu¹ · Bin Wang^{1,2} · Yingchao Xu¹ · Liang Wang³ · Wenqin Cheng¹

Received: 10 April 2020 / Accepted: 12 July 2020 / Published online: 29 July 2020
© The Indian Institute of Metals - IIM 2020

Abstract This study investigated the fatigue crack propagation (FCP) behavior of different regions (base metal (BM), heat-affected zone (HAZ) and weld metal (WM)) of dissimilar metal welded joints of L360MS pipeline steel with Inconel 625 welding wire as the filler material. The effect of the microstructure on FCP was discussed. The results indicated that the fatigue crack growth rates (da/dN) for the WM were lower than those for the BM and the HAZ under the same stress ratio. The microstructures of these regions had different characteristics, such as equiaxed austenite, ferrite and pearlite, which could explain the observed differences in properties. For instance, the FCP

path revealed that the existence of ductile equiaxed grains and coarse columnar grains caused the WM to have higher fatigue crack growth resistance and a more tortuous crack propagation path than the BM and the HAZ. The microstructure, grain orientation, strain distribution and grain boundaries around the fatigue crack in the HAZ specimens that propagated through the WM and the fusion line were analyzed by electron backscatter diffraction (EBSD). The results showed that the fatigue cracks followed a zigzag path into the HAZ along the high-angle Type II boundary and Type I boundary in the WM.

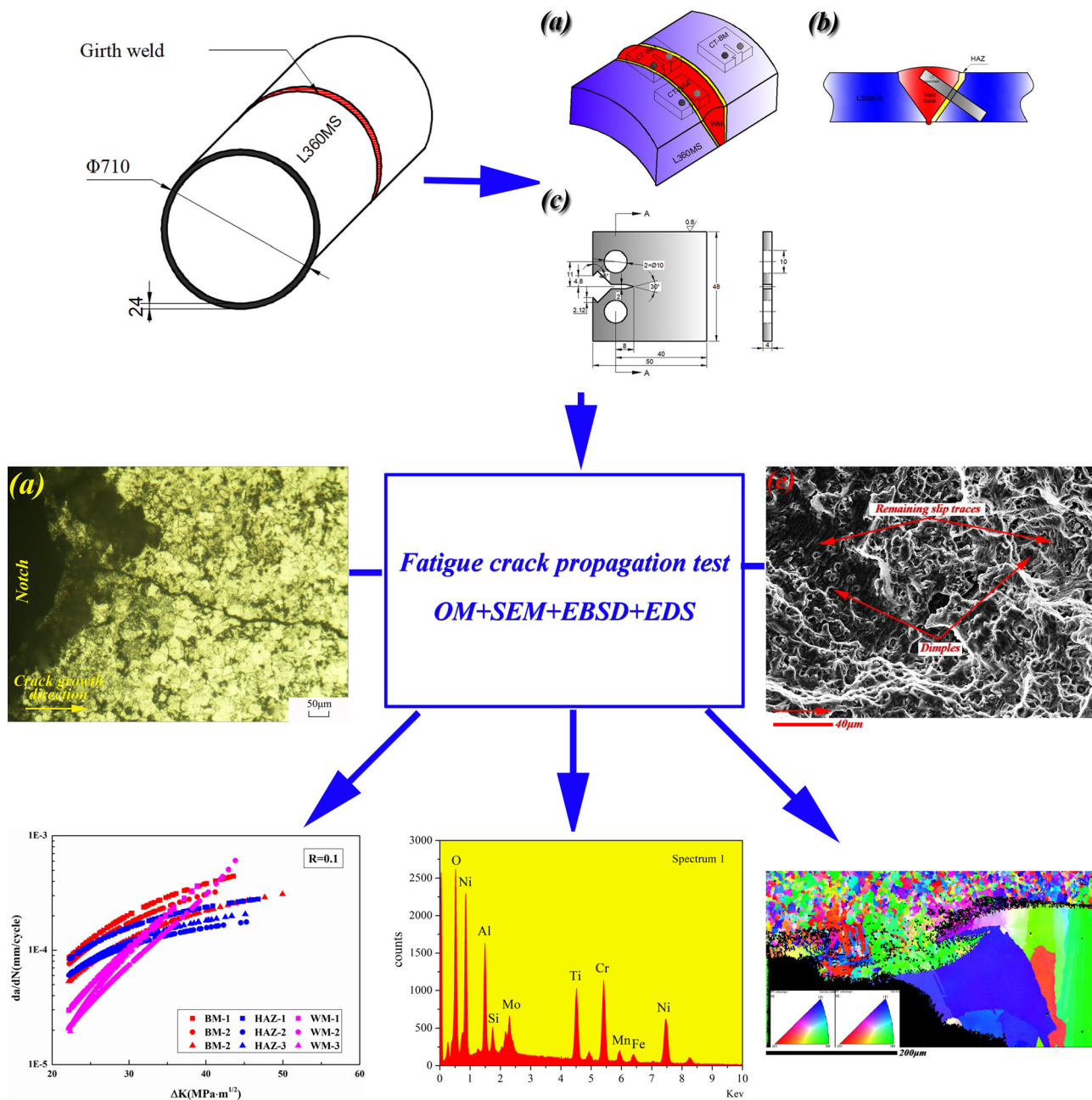
✉ Bin Wang
wangbincn89@163.com

¹ School of Materials Science and Engineering, Southwest Petroleum University, Chengdu 610500, China

² Welding Engineering Technology Research Center in Sichuan Province, Chengdu 610500, China

³ School of Engineering, Southwest Petroleum University, Nanchong 637800, China

Graphic Abstract



Keywords Dissimilar metal welded joint · Fatigue crack propagation · Bimetallic composite pipe · EBSD

1 Introduction

As energy consumption is increasing worldwide, energy resources are facing depletion, and it is increasingly difficult to exploit traditional energy resources such as oil and

natural gas. Extreme extraction and transport environments have imposed strict requirements on transport pipelines, wherein the general aim is to minimize cost while ensuring the transport quality. Bimetallic composite pipes (BCPs) have become a research focus because of their good corrosion resistance, mechanical properties and processability, which can significantly improve the service life of pipelines [1–3]. The combination of low cost and superior performance has led to the wide adoption of BCPs in oil and gas transport, the chemical industry, the nuclear industry and other fields [4–8].

For BCPs, stainless steel or nickel-based alloys mainly provide corrosion resistance and are used as the cladding layer. Carbon steel or high-strength low-alloy steel as the base layer mainly provides strength. Fatigue fracture is a common failure form of oil and gas transmission pipelines in service [9, 10]. Transport pipelines will inevitably be subjected to alternating loads during service. Some of these alternating loads come from the pressure fluctuations in the conveying medium and the layered structure of oil and gas flow in the pipeline, whereas other alternating loads come from outside of the pipeline, such as vibrations caused by vehicles passing above the buried pipeline, vibrations caused by geological migration, and Kaman vibrations caused by fluid impacts when the buried depth of the pipeline is insufficient. These alternating loads impose higher requirements on the base layer that provides strength support, especially for the welded joints of the base layer. Moreover, due to the microstructure and chemical composition differences, a weak area that is prone to cracking exists in the base layer metal and the dissimilar welded joints. Therefore, understanding the crack propagation behavior in each region of the base layer, dissimilar metal welded joint (DMWJ) is of great significance to the integrity and safety design evaluation of a BCP. However, the failure of a DMWJ is a complicated process due to the microstructure and operating environment. Although many studies have been carried out on the microstructure [11–13], strength [14–16], fracture [17–27] and stress corrosion cracking [28–34] of DMWJs, few reports have analyzed the crack propagation behavior of DMWJs in BCPs.

There are few reports on the FCP behavior of DMWJs. Cortés et al. [35] studied the crack growth behavior of Inconel 718 and AL6XN DMWJs filled with ERNiFeCr-2. The crack propagation rate of the WM was considered to be the highest under the influence of brittle second phases such as Laves and NbC. Wang et al. [36] studied the crack formation and propagation of DMWJs in L360QS low-carbon steel and N08825 nickel base alloy composite pipes. They found that the crack was formed in the nickel base alloy layer and subsequently propagated perpendicular to

the fusion zone and terminated in the weld. Jang et al. [37] studied the effect of microstructure and residual stress on the FCG rate of narrow-gap DMWJs. Because of the presence of tensile residual stress, the fatigue cracks first expanded along γ -austenite dendrites, and the propagation speed was accelerated at the root of the weld. Wang et al. [38] studied the effect of the local microstructure on the initiation and propagation of short cracks in various regions of the DMWJs in a nuclear power plant. Due to the presence of second-phase particles at grain boundaries, the cracks tended to germinate in the slip zone and propagate along columnar grain boundaries. The fracture mode of the WM was intergranular fracture. Ki et al. [39] determined the FCG rate of various parts of A508/alloy82/316L DMWJs and found that the residual compressive stress helps to slow the rate of crack propagation at the interface of the WM. Huang et al. [33, 40] also simulated the effects of residual tensile stress, crack closure and heat treatment on the FCG of corroded DMWJs.

The present work studies L360MS/N08825 BCPs filled with Inconel 625, wherein the particular focus is on the BCP base layer and WM of the welded joint. Accordingly, FCG rate tests were carried out on various regions of girth welds of CT specimens in an atmospheric environment. An optical microscope (Olympus Corporation, Japan) and a scanning electron microscope (Thermo Fisher, the USA) equipped with an energy-dispersive spectrometer were used to observe and analyze the FCP path and fatigue fracture in various regions to understand the fracture characteristics of the joint and reduce the potential safety risks (Table 1).

2 Experimental Procedure

2.1 Materials

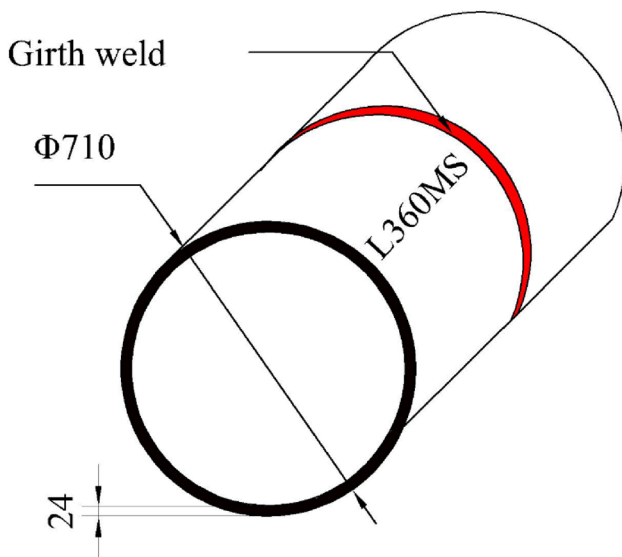
The materials used were L360MS/N08825 BCPs, which were formed by centrifugal casting. The BCPs were welded together using tungsten inert gas welding (TIG), and the welding process and parameters were reported in our

Table 1 Chemical compositions of N08825, L360MS and Inconel 625 (wt%)

	C	Si	Mn	P	S	Nb	Ti
N08825	0.022	0.14	0.47	0.012	–	–	–
L360MS	0.10	0.45	1.65	0.025	0.003	0.06	0.04
Inconel625	0.03	0.40	0.30	0.01	0.01	3.7	0.03
	V	Cu	Ni	Cr	Mo	Al	Fe
N08825	–	1.47	41.14	22.07	313	–	Bal
L360MS	0.05	–	–	–	–	–	Bal
Inconel625	–	0.03	61.60	22.00	8.70	0.1	Bal

Table 2 Fatigue crack growth rates

Region	Equation of fatigue crack growth rate	Correlation coefficient
BM	$da/dN = 5.4641 \times 10^{-8} (\Delta K)^{2.3524}$	0.9873
HAZ	$da/dN = 4.0829 \times 10^{-7} (\Delta K)^{1.6899}$	0.9843
WM	$da/dN = 3.4867 \times 10^{-11} (\Delta K)^{4.3736}$	0.9952

**Fig. 1** Schematic diagram of the L360MS pipeline steel

previous paper [36]. The chemical compositions of the N08825, L360MS and Inconel 625 filler metals are given in Table 2. After welding, all joints were kept at 600 °C for 3 h and then cooled in a furnace to release residual stresses. Finally, the welded joints were subjected to X-ray and ultrasonic nondestructive testing, and the N08825 cladding layer was stripped after there were no defects. The specifications of the $\Phi 710$ mm \times 24 mm L360MS pipeline steel are shown in Fig. 1.

2.2 Metallographic Observations and Hardness Measurements

The specimens encompassing the BM, WM and HAZ in the welded joint were sampled for metallographic observations with a DME200M optical microscope, elemental analyses with a scanning electron microscope/energy-dispersive spectrometer instrument, and hardness measurements with an HXD-2000TM/LCD microhardness tester. The specimens were polished and etched (the BM and HAZ were etched in 4% nital solution, whereas the WM was etched in aqua regia) before the examinations, and the results revealed the material properties.

2.3 Fatigue Test Procedures and Characterization

The FCG test was conducted in accordance with ASTM E647-15, “Standard Test Method for Measurement of Fatigue Crack Growth Rates.” The FCG rate was tested by standard compact tension (CT) specimens. The crack tips were located at the BM, HAZ and WM. The method of taking specimens from the welded joint and the details of the CT specimen are shown in Fig. 2, and no less than 3 specimens were used for each group. A PWS-50 electrohydraulic servo dynamic test system was used for the test, which was conducted at 25 °C (room temperature). All specimens had 2-mm-long prefabricated cracks, and the specimens were cyclically loaded under sinusoidal load control with a frequency $f = 8$ Hz, a load ratio $R = 0.1$ and a maximum load of 4.5 kN while keeping the other test parameters unchanged after crack prefabrication. Moreover, FCP tests with $P_{\max} = 4$ kN and $P_{\min} = 0.4$ kN were carried out. The specimen FCP path was characterized under optical microscopy (OM) after the fatigue experiment. Afterward, electron backscatter diffraction (EBSD) analysis was performed on an FEI Nova NanoSEM 430 equipped with HKL Channel 5 software, which was used to characterize the cracks in the HAZ specimens that propagated across the interface. The scanning region size was $240 \mu\text{m} \times 500 \mu\text{m}$, and the scanning step length was $0.6 \mu\text{m}$. The fracture surfaces after the FCP tests were observed by scanning electron microscopy (SEM).

3 Results and Discussion

3.1 Microstructure and Microhardness

Figure 3 shows the micrographs of various regions of the welded joint and a scan of the weld interface. Figure 3a clearly shows the microstructure of dissimilar welded joints composed of the BM, HAZ and WM. The microstructure of the BM consists of banded pearlite and ferrite (Fig. 3b). The microstructure of the superheated zone (Fig. 3c) near the FL is abnormally coarse. The coarse-grained zone is composed of coarse ferrite, pearlite and lath martensite, and the microstructure of the fine-grained zone is similar to that of the BM. Two boundary

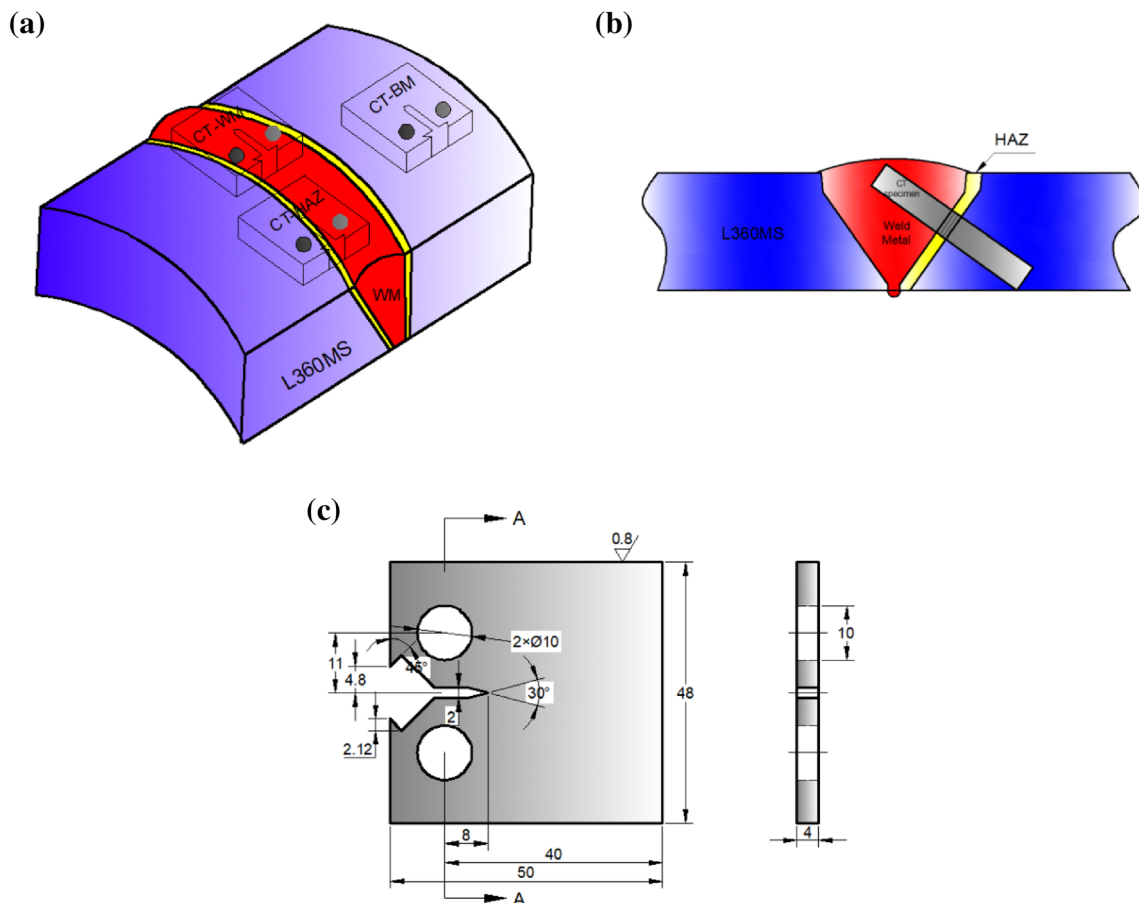


Fig. 2 a Sampling position of the CT specimens. b Schematic diagram of the notch position in the HAZ specimens. c Schematic diagram and size of the CT specimen sampling location

types can be clearly seen in the figure: the Type II boundary, which is approximately 20–50 μm from the FL, and the equiaxed grain boundary Type I boundary, which connects the Type II boundary and the FL (Fig. 3d). Previous studies [41–44] have shown that the formation of these two boundaries is related to the difference in the grain structure between the BM and the WM and the rapid change in chemical composition on both sides of the FL. Among them, the Type I boundary is the result of epitaxial grain growth, whereas the Type II boundary is caused by the change in the solidification mode of the molten pool. These two types of grain boundaries are high-angle grain boundaries, which are highly sensitive to stress corrosion cracking (SCC) and easily become crack initiation sites and crack propagation paths [13, 44]. In addition, the microstructure of the WM is columnar austenite and equiaxed austenite (Fig. 3d).

Figure 3e shows an SEM image and the energy-dispersive spectroscopy (EDS) line scan results of the weld interface. The concentrations of the main elements—Fe, Ni, Cr and S—in the WM shows that there is an obvious abrupt change region on both sides of the FL. Because the

alloy element in the WM is diluted and the Fe content is increased by the BM melting during welding, the content of each element in the WM far away from the FL slowly returns to the normal level. Another significant change appears on the Type II boundary: The contents of Fe and Cr decrease slightly, whereas the contents of Mo, Nb and S increase sharply. A decrease in the content of Cr means a decrease in the corrosion resistance, and a high content of Mo (> 3%) will worsen the oxidation resistance of steel. Nb has a strong affinity for O, C and N and easily forms stable compounds. The accumulation of S confirms the lack of corrosion resistance of the Type II boundary.

The microhardness distribution of the entire welded joint interface region is shown in Fig. 4. The hardness of the BM is lower than that of the WM, and the hardness of the WM fluctuates greatly. The hardness of the filling layer is higher than the hardness of the root layer due to temper softening during the welding process. In addition, there is a region of hardness increase at the interface between the WM and the BM. Related research [45, 46] shows that this is due to the existence of a carbon-rich zone in the weld layer near the FL, which provides strong solid solution

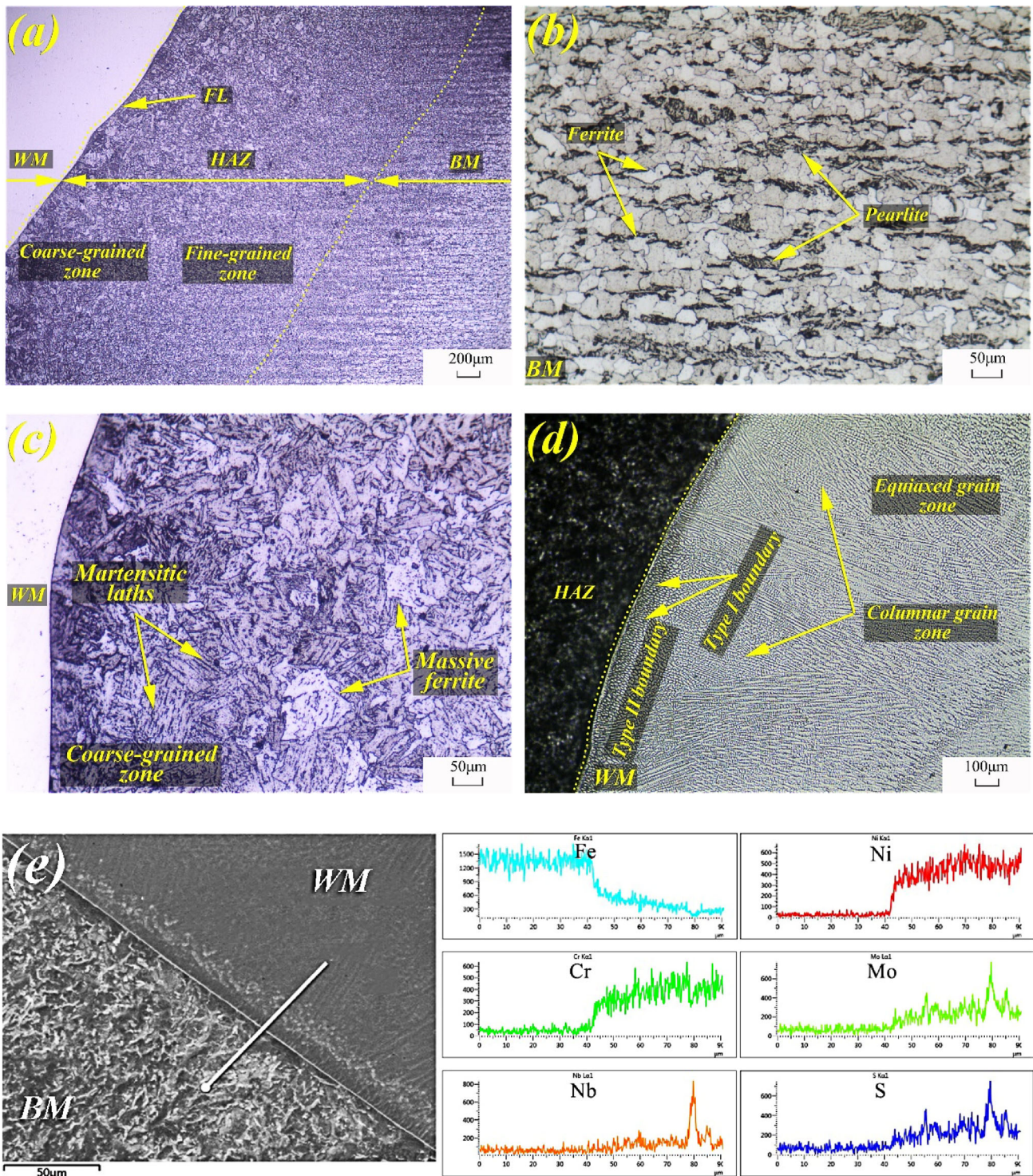


Fig. 3 OM micrographs of **a** the whole welded joint, **b** the BM, **c** the coarse-grained zone and **d** the WM. **e** SEM micrograph and EDS line scan results of the weld interface

strengthening and produces a martensite-like structure. The lowest hardness value in the weld is adjacent to the highest hardness point, which is caused by the weakening of the solid solution strengthening by the migration of Ni and Cr

to the parent metal [47]. A relative hardness decrease occurs on the HAZ side of the FL, and the local softening in this region is due to high-temperature tempering during the welding process.

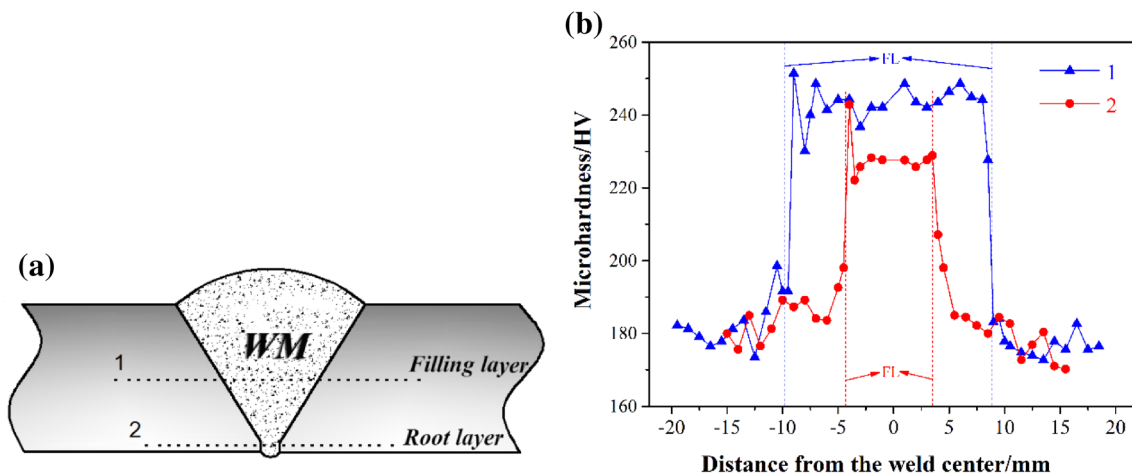


Fig. 4 a Distribution of hardness measuring points on the welded joint. b Microhardness profile across the welded joint

3.2 Fatigue Crack Growth Rate

In this study, the data (a, N) are processed by the Smith method [48] when calculating the FCG rate, i.e., da/dN . The Smith method is based on a group of functions, as shown in Eq. (1). The FCG rate obtained by the Smith method reflects the overall FCG rate:

$$y_i = B_0 + B_1 \ln x_i + B_2/x_i \tag{1}$$

$$\frac{da_i}{dN_i} = \frac{a_i^2}{(B_1 a_i - B_2 a_1)} \tag{2}$$

$$\Delta K = \frac{\Delta P}{B\sqrt{W}} \cdot \frac{(2+\alpha)}{(1-\alpha)^{3/2}} (0.886 + 4.64\alpha - 13.32\alpha^2 + 14.72\alpha^3 - 5.6\alpha^4) \tag{3}$$

where $y_i = N_i - N_1$ (N_i is the number of real-time cycles), $X_i = a_i/a_1$ (a_i is the real-time crack length), and B_0, B_1 and B_2 are the undetermined coefficients that can be obtained by regression of the test data.

The FCG rate is obtained by taking the derivative of Eq. (1).

The crack tip stress intensity factor range ΔK corresponding to the FCG rate da/dN is calculated by using the crack length a_i . For the CT specimens, ΔK is determined by Eq. (3).

ΔP is the amplitude of the applied load and $\alpha = a/W$ ($\alpha \geq 0.2\alpha$).

The steady-state crack growth (stage II) rate can be expressed as the following Paris law:

$$\frac{da}{dN} = C(\Delta K)^n \tag{4}$$

where C and n are material constants that are determined from experiments.

According to the curve of da/dN vs ΔK in various regions of the welded joint (Fig. 5), each crack propagation curve can be divided into stages I and II (initiation and Paris stage). Because of the nonuniformity of the microstructure of the material, the fatigue crack growth rate has a large amount of scatter. These results also indicate that the FCG rates in various regions of the welded joint are different and that the crack growth rate increases as the number of cycles increases under the same stress ratio. The rate is lower during stage I of crack propagation, where crack propagation is faster in the BM and HAZ and slower in the WM. In stage II, at low ΔK , the FCG rate trend is comparable to that in stage I; however, as ΔK increases, the differences in the FCG rates in various regions decrease.

The equation of steady-state FCG rates in various regions of the welded joint is shown in Table 2.

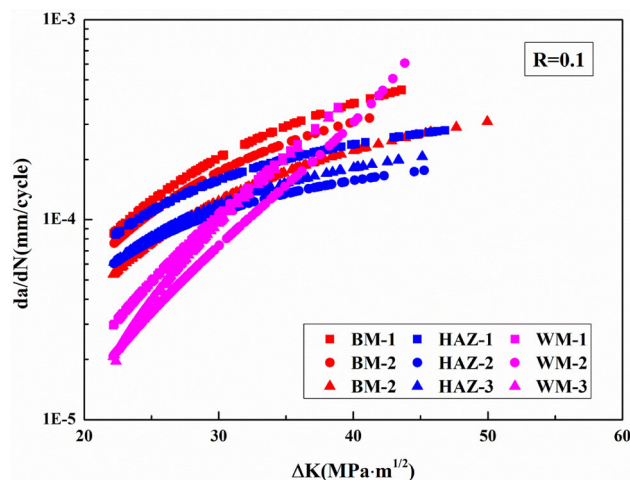


Fig. 5 L360MS pipeline steel fatigue crack growth rate in various regions of the welded joint

3.3 Fatigue Crack Propagation Path in Various Regions of the Welded Joint

3.3.1 Fatigue Crack Propagation Path in the BM

Figure 6 shows a micrograph of the FCP paths in the BM. Figure 6a corresponds to the precrack, in which the crack originates at a high stress concentration point near the machined notch and then propagates in a tortuous manner along an approximately straight line. As shown in Fig. 6b, c, when ΔK is low, the grain boundaries may hinder FCP, and the crack mainly propagates along the grain boundaries

of ferrite and pearlite, following the principle of minimum energy consumption [49]. The crack bypasses the harder inclusions in the structure (Fig. 6b) and the hard pearlite (Fig. 6c). When ΔK is high, the fatigue crack mainly propagates transgranularly. In Fig. 6d, the crack directly propagates through the soft ferrite phase.

Figure 6e shows a schematic diagram of the principle of FCP in the BM, which is in agreement with the study by Guan et al. [50]. The second hard phase, pearlite, plays an important role in deflecting the FCP path and hindering FCP. In addition, the crack can also pass through the pearlite in some cases, depending on the orientation of the

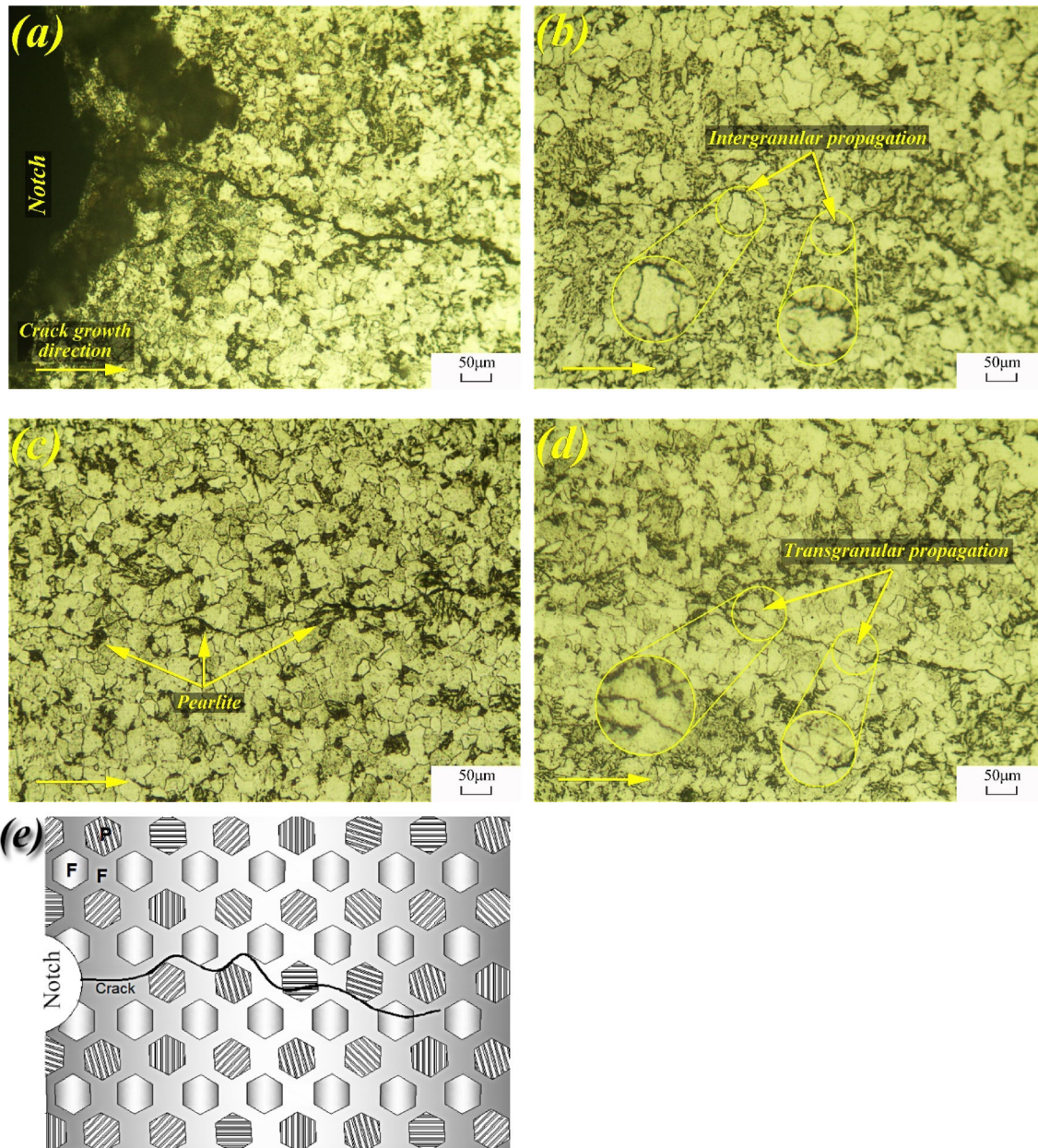


Fig. 6 OM images of the crack growth paths in the BM: **a** crack growth path from the precrack and **b–d** stable crack propagation path (ΔK increases gradually). **e** Schematic diagram of the fatigue crack propagation principle in the BM

pearlite lamellae. When the crack tip is parallel to the pearlite lamellae, the crack will transgranularly propagate within the pearlite; otherwise, the crack will bypass the pearlite.

3.3.2 Fatigue Crack Propagation Path in the WM

Figure 7 shows a micrograph of the FCP paths in the WM. From the fatigue crack initiation region (Fig. 7a, b), it is observed that the initial crack/slip surface is oriented at an angle of 45° with respect to the loading axis because the

WM structure is equiaxed austenite with 12 slip systems. When subjected to external forces, slip can only occur in the direction that is most conducive to the occurrence of slip [51, 52]. Because the shear stress plays a leading role in the process of fatigue crack initiation, the soft orientation of slip is preferred. During the stable propagation period of fatigue cracks (Fig. 7c–e), it can be seen that when ΔK is low, the crack propagates along an approximately straight line through the WM equiaxed grain region, and the propagation direction is perpendicular to the load direction. When ΔK is higher, the FCP path begins to

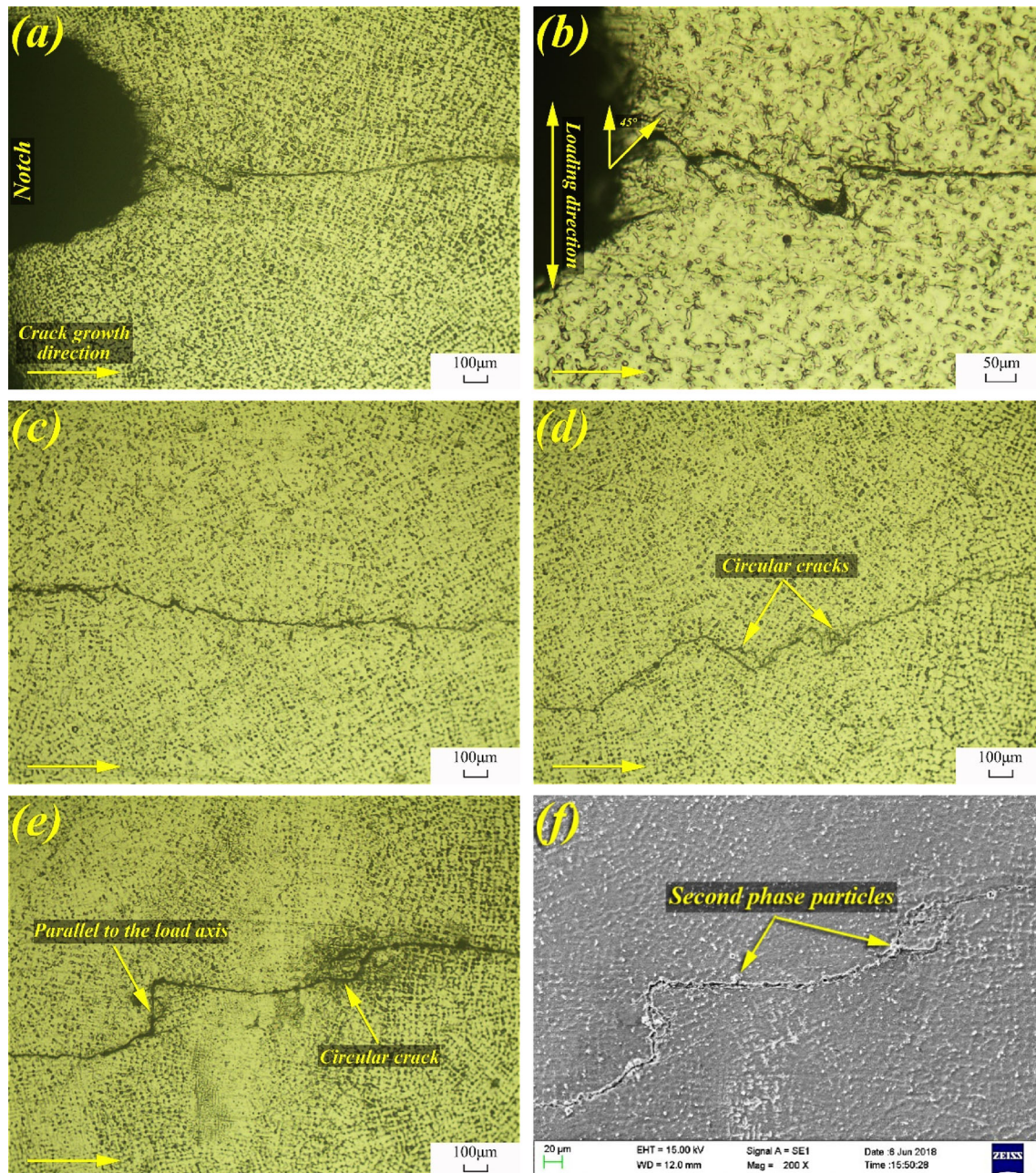


Fig. 7 OM images of the crack growth paths in the WM: (a, b) crack growth path in the crack initiation region and c–e stable crack propagation path (ΔK increases gradually). f SEM image of the region shown in (e)

become tortuous, accompanied by bifurcation and even circular cracks. This phenomenon will slow the FCP rate and produce a small amount of plastic deformation around the crack [53]. The SEM image (Fig. 7f) in Fig. 7e shows that there are a large number of fine second-phase particles around the crack, which are dispersed on the austenite grain boundary. The second-phase particles maintain a coherent or incoherent relationship with the matrix, which can often hinder the movement of dislocations [54]. Moreover, the majority of the second-phase particles gather at the junction of multilayer and multipass welding where the tortuous fatigue cracks occur, indicating that the second-phase particles have a great hindering effect on FCP. Therefore, it can be concluded that the WM has good fatigue crack resistance.

3.3.3 Fatigue Crack Propagation Path in the HAZ

Figure 8 illustrates a micrograph of the FCP paths in the HAZ, wherein the fatigue crack is formed at the notch in the specimen and then propagates approximately parallel to the fusion line (Fig. 8a, b). By analyzing the microstructure of the welded joint (Fig. 3), the FCP paths in the HAZ

specimens are in the fine-grained zone of the welded joint. The area is normalized during the welding thermal cycle, its microstructure is composed of fine pearlite and ferrite, and the mechanical properties are superior to those of the parent metal. This explains why the FCG rate of some HAZ specimens in Sect. 3.1 is slightly lower than that of the parent metal. The whole crack propagates along a straight line, and the crack growth path is tortuous and accompanied by crack branches (Fig. 8c, d). However, the tortuosity of cracks in the HAZ specimen is different from that of the cracks in the BM specimen: In the HAZ specimen, the cracks have many small tortuous regions, wherein the tortuosity is more substantial than that of the cracks in the BM, and there are more crack branches. The crack bifurcation phenomenon is rare in the BM specimens. However, compared with the FCP path in the WM, the tortuosity of the crack in the HAZ specimen is smaller, and the FCP resistance of the WM is higher.

3.3.4 EBSD Analysis of the HAZ

During the observation of the FCP path in the HAZ specimen, the crack in one of the specimens propagates across

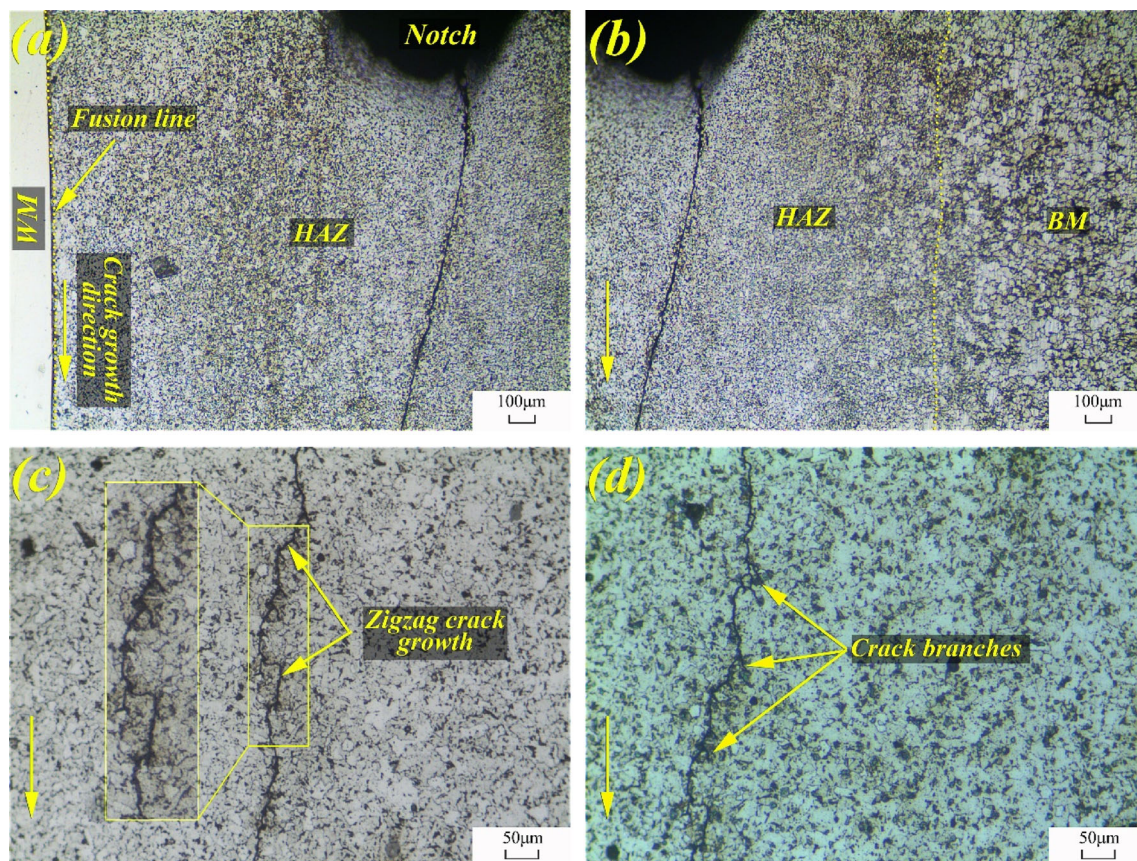


Fig. 8 OM images of the crack growth paths in the HAZ: **a, b** crack growth path in the crack initiation region and **c, d** stable crack propagation path (ΔK increases gradually)

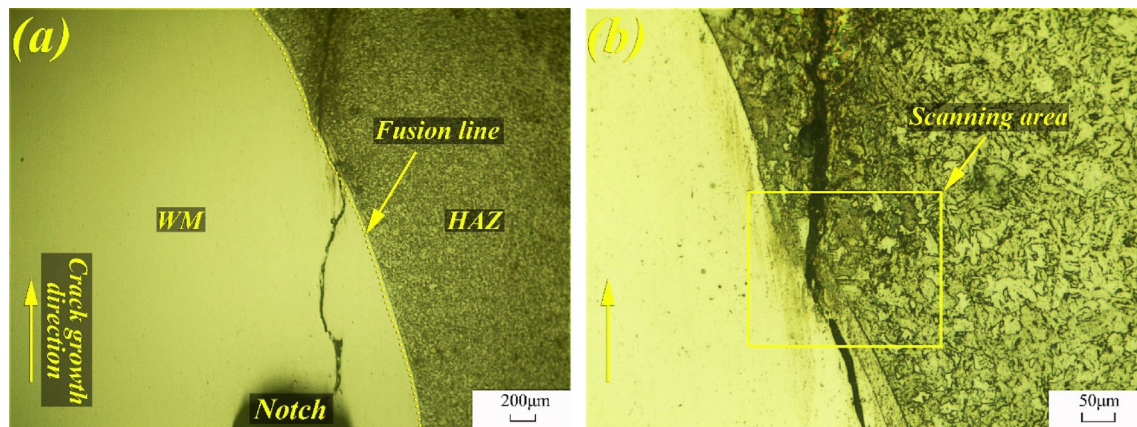


Fig. 9 OM images of **a** fatigue crack propagation across the interfaces in the HAZ specimens and the **b** scanning area

the interface (Fig. 9). After the fatigue crack forms at the specimen notch, it first tortuously propagates forward in the welding seam, extends a short distance parallel to the FL after approaching the FL and then passes through the FL and enters the HAZ. According to the microstructural analysis of the WM near the FL in Fig. 3d, it can be assumed that the fatigue crack encounters the Type II boundary in the WM during propagation, and the Type II boundary itself has a high SCC sensitivity.

It is of great significance to study the relationship between the FCP and the microstructure, grain orientation, grain boundary distribution and strain distribution, which can provide important information on crack growth anomalies in this region. During this period, the crack is scanned and analyzed from the point of view of crystallography via the EBSD technique.

EBSD maps are presented in Fig. 10, and the image quality map (Fig. 10a) well reflects the granular grains in the BM and the columnar grains in the WM. As shown in Fig. 10b, the fatigue crack propagates from the face-centered cubic (FCC) austenite to the body-centered cubic (BCC) ferrite and pearlite.

The FCP process is bound to produce a large amount of plastic deformation, resulting in dislocations and dislocation interfaces, and the EBSD technique can measure the grain orientation change caused by a large number of dislocation arrangements. The orientation relationship of the microstructure around the crack is clearly reflected by the inverse pole figure (IPF) after software processing (Fig. 10c). The columnar grains of the WM have obvious directionality, and the misorientation is small. With preferred orientation, the crack propagates along the edge of a large cluster of grains with the same or similar orientation, and this region corresponds to the Type I boundary. The microstructure orientation on the HAZ side is more confusing.

As shown in the kernel average misorientation (KAM) map (Fig. 10d), except for many strain regions caused by

the influence of the welding thermal cycle on the HAZ, there is no large strain zone around the crack in the WM. This may be due to the propagation of fatigue cracks along the path with lower resistance (along the Type I boundary). Near the FL, a high degree of stress concentration (large range of yellow areas) can be found, indicating that there is a higher density of dislocation pileup in this area and that crack propagation in this area is difficult. Hence, the crack bypasses this region and enters the HAZ.

The grain boundary distribution map of Fig. 10e confirms that the fatigue crack propagates along the high-angle grain boundary in the WM (corresponding to the Type I boundary) and enters the HAZ; because of the low crack propagation resistance at the Type I boundary, there is no large strain region around the crack.

By analyzing the OM images and EBSD results of the fatigue cracks in the HAZ specimen, a schematic diagram of the HAZ FCP model can be created (Fig. 11). This model is consistent with the stress corrosion cracking mechanism of alloy 182 and A533B low-alloy DMWJs in PWR nuclear power plants studied by Hou et al. [13]. When subjected to a high-temperature and high-pressure water environment, fatigue cracks are generated from the notches machined in the CT specimens, and these cracks exhibit tortuous propagation in the WM until they encounter the Type II boundary near the FL. These cracks continue to extend along the Type II boundary with low resistance to crack propagation for a short distance, and then they reach the FL through the Type I boundary and finally enter the HAZ under external forces.

3.4 Fatigue Fractography

3.4.1 BM and HAZ

Because the BM and the HAZ have the same ferrite + pearlite microstructure, the fracture surfaces of the BM and the HAZ are very similar. The crack growth rate in

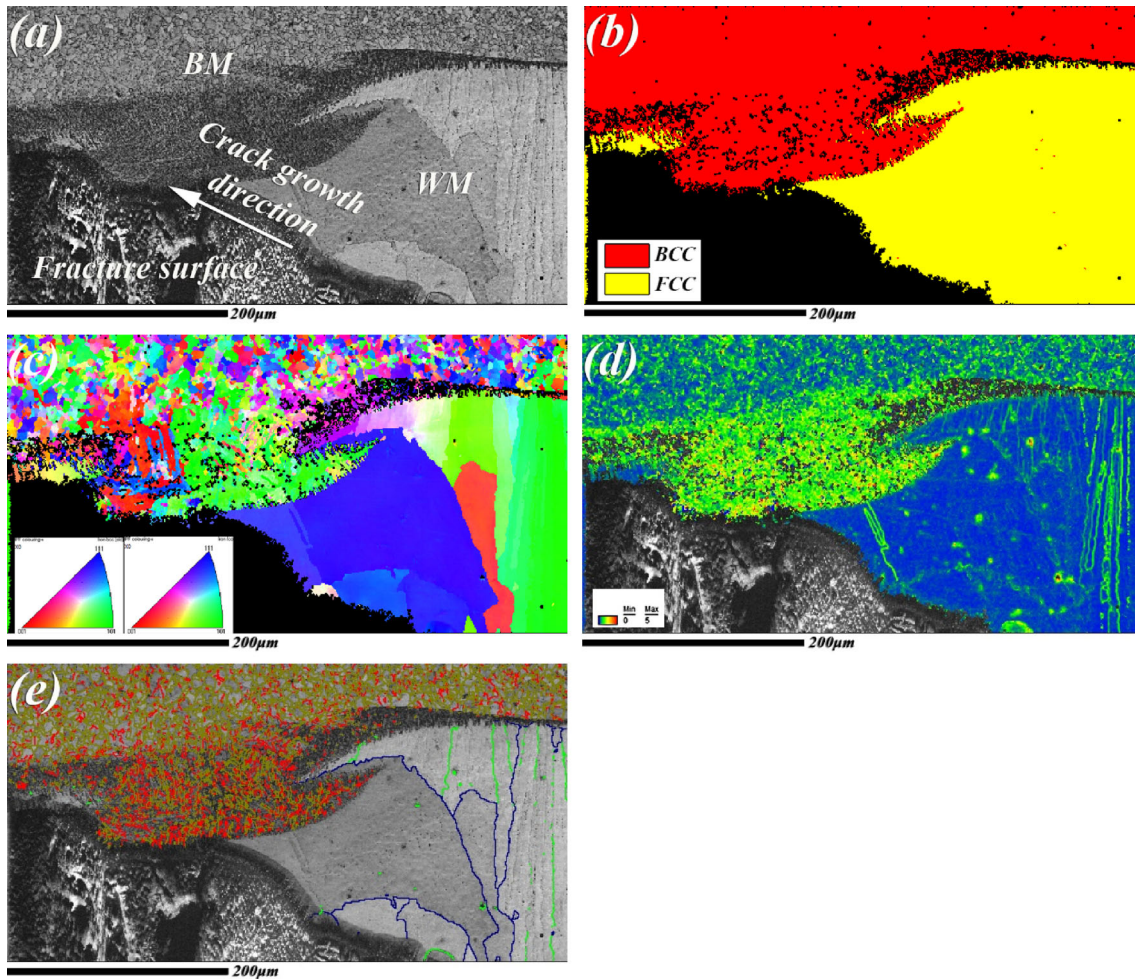


Fig. 10 EBSD maps: **a** image quality map, **b** phase map, **c** IPF map, **d** KAM map, **e** high-angle grain boundary (represented by blue line) and low-angle grain boundary (represented by red line) distribution map (color figure online)

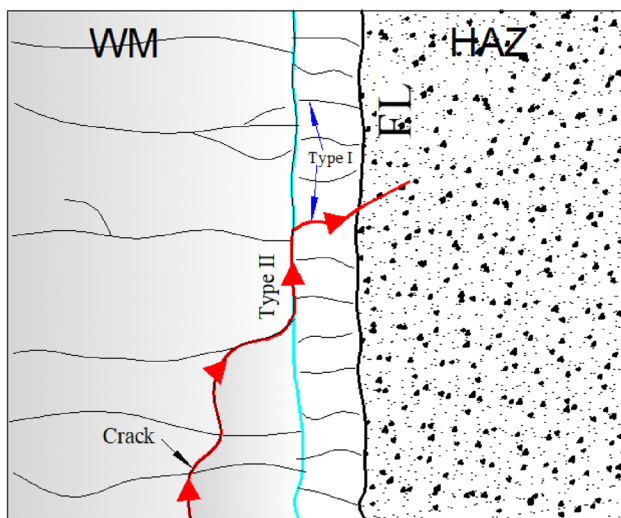


Fig. 11 Schematic diagram of the HAZ fatigue crack propagation model [13]

the initial crack growth period (Fig. 12a, b) is low, and the corrosion layer formed by the full contact between the air and water in the environment and the crack tip fracture surface results in the dark color of the fatigue source region. After the crack enters the stable propagation period (Fig. 12c, d), a large number of fatigue steps appear on the fracture surface, accompanied by many secondary cracks (Fig. 12e), and no fatigue striations are observed. The fatigue step is not only strong evidence for the increase and advancement of cracks between cleavage planes but also an important index to reflect the crack resistance in the structure. Moreover, the fatigue steps in Fig. 12c are much larger than those in Fig. 12d. This analysis shows that for the ferrite + pearlite structure, when the crack grows from the brittle pearlite to the ductile ferrite, the crack growth slows due to the sudden increase in resistance. The grain size also has a certain influence on the crack growth rate. The refinement of the structure not only greatly improves its yield strength but also greatly increases its plasticity,

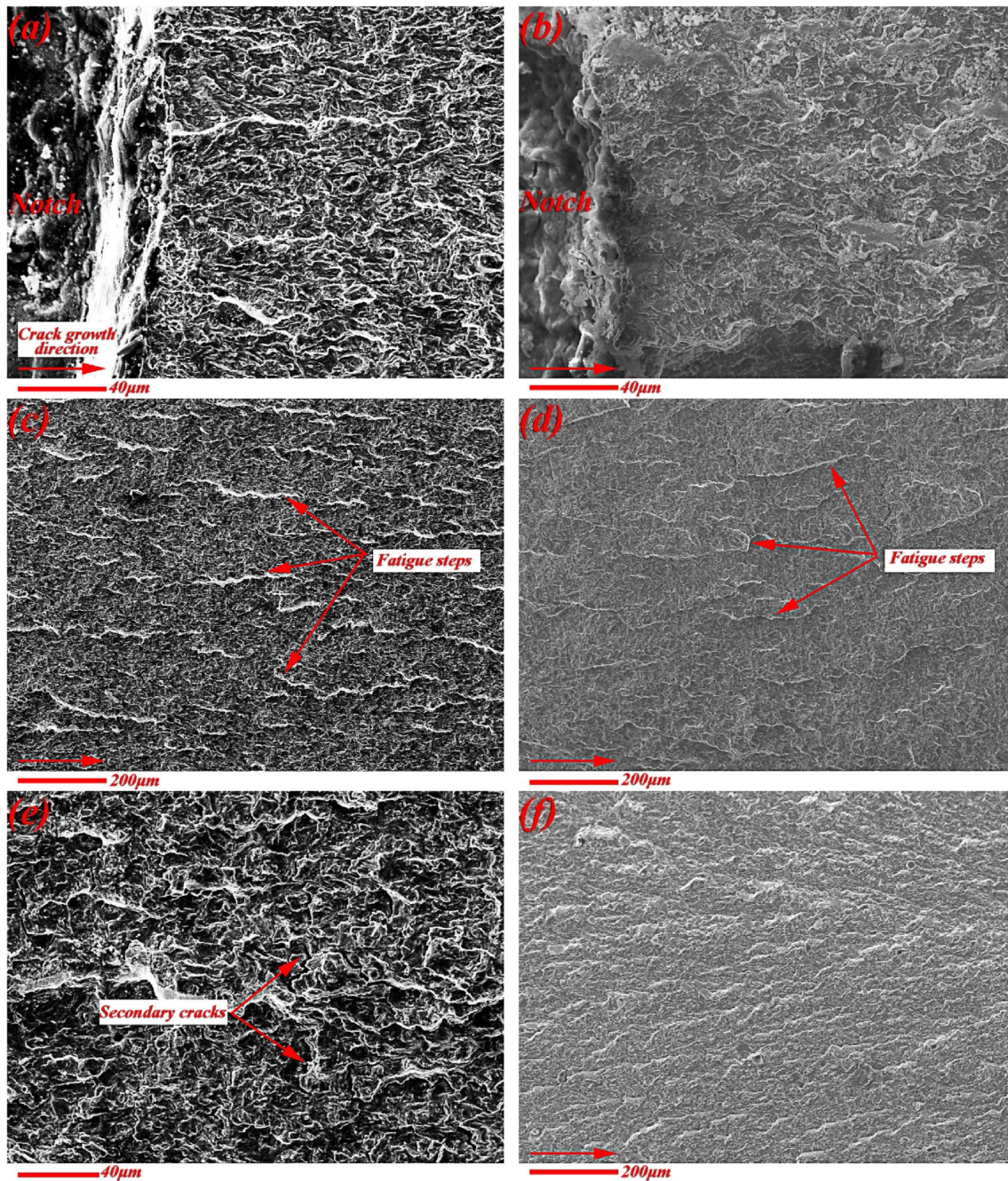


Fig. 12 SEM fractographs of the BM and the HAZ: **a** crack initiation region in the BM, **c**, **e** crack stable propagation region in the BM (ΔK increases gradually), **b** crack initiation region in the HAZ, and **d**, **f** crack stable propagation region in the HAZ (ΔK increases gradually)

thereby making it more difficult for the material to crack. Compared with the fine-grained region of the HAZ, the BM grains are coarser and the crack resistance is smaller, which is more conducive to sliding. Some slip surfaces with approximately the same orientation meet to form a large slip surface, and more slip surfaces with different orientations meet and interact to form a fatigue step. The secondary crack is beneficial to slow the crack propagation

rate. The rapid propagation period of the fatigue crack in the HAZ (Fig. 12f) is similar to the radial region of tensile fracture, and there are a large number of radial patterns, indicating that the plasticity of this HAZ structure is poor; the direction of the radial patterns is parallel to the direction of the crack propagation and points back to the crack source. However, this phenomenon was not observed in the BM specimens.

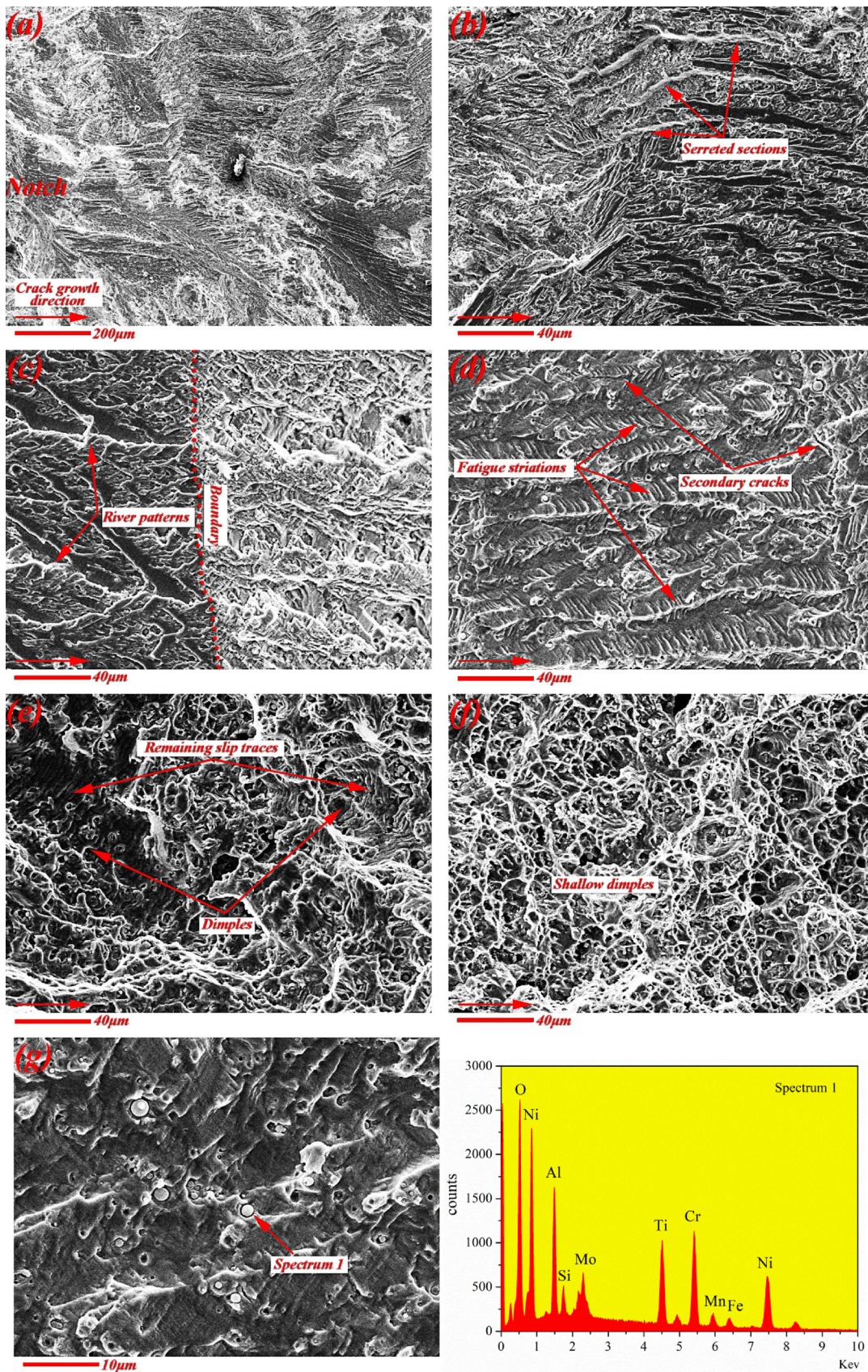


Fig. 13 SEM crack fractography of the WM: **a** crack initiation region and **b–f** stable crack propagation region (ΔK increases gradually). **g** EDS results of the inclusions in the fatigue-fractured WM specimen

3.4.2 WM

Figure 13 shows the SEM images of the fatigue fracture of the WM specimens. The fracture morphology of fatigue crack initiation and early propagation period (Fig. 13a, b) and the WM FCP path (Fig. 8) show that the crack propagates in the pure shear mode, mainly along the direction of the main slip system. A large number of cleavage fracture characteristics, such as river patterns and tear ridges, are found on the fracture surface [55].

When the fatigue crack enters the stable propagation period (Fig. 13c, d), an obvious dividing line can be found between the prefabricated crack and the test crack (Fig. 13c). Compared with the precrack test, the loading force of the test decreases, the driving force ΔK of crack propagation is already very large, the crack growth rate is relatively fast, the fatigue fracture becomes rough, and the gloss brightens. From the fatigue striations found on the fracture surface (Fig. 13d), it can be concluded that the fracture is a fatigue fracture [56]. The fatigue striations are not continuous and exist on different sections, and the spacing between striations becomes wider as ΔK increases. The smaller the spacing of fatigue striations is, the better the fatigue performance is and lower the FCP rate is. Both the BM and the HAZ are BCC structures. Because the metal with a BCC structure has many slip systems and high stacking fault energy and is prone to staggered slip, it is more difficult to form fatigue striations in this metal than in the metal with an FCC structure. Moreover, the secondary crack on the fracture surface is basically parallel to the fatigue striation, which indicates that during the crack growth process, austenite has better crack growth resistance than ferrite and pearlite.

With the increase in ΔK , the number of fatigue striations on the fracture surface decreases gradually (Fig. 13e), and a considerable number of micropores appear. These micropores are actually formed by impurities or second-phase particles being peeled off from the matrix under cyclic stress. The EDS analysis of the inclusions, as shown in Fig. 13g, shows that the main components of the spherical inclusions are oxides of Al and Ti. Under the action of an external force, these inclusions tend to produce greater stress concentrations, and when they meet with cracks, crack propagation is promoted by the inclusions or their cracking boundaries. Although there are also holes in the stable crack propagation zone, the number of cracks is small, and the size of these cracks is small. Under the action of stress, these micropores continue to grow through plastic deformation and finally form dimples. Figure 13e

shows that some micropores have grown into dimples, and signs of slip can also be clearly seen at the edge of the dimples, which indicates that when the fatigue crack enters the rapid propagation zone, it follows the slip mechanism and dimple formation mechanism. As ΔK increases, the stress intensity factor K reaches the critical value K_{IC} , the crack enters the unstable propagation region, and the FCP is controlled by a single dimple formation mechanism, exhibiting typical ductile fracture characteristics, as shown in Fig. 13f.

4 Conclusions

The microstructure and fatigue properties of L360MS pipeline steel welded joints were studied by OM, SEM and fatigue tests. The FCP behavior of specimens in different regions was analyzed and studied, and the following conclusions were drawn from the results:

- (1) In L360MS pipeline steel welded joints, the BM was composed of banded pearlite and ferrite, the WM included columnar and equiaxed austenite, and the Type I boundary and Type II boundary appeared near the FL. The HAZ included a coarse-grained zone, which was composed of coarse ferrite, pearlite and lath martensite, and a fine-grained zone, which was composed of fine ferrite and pearlite.
- (2) The a - N curves of the specimens and the FCG rate equations for the different regions of the specimens were fitted. Under the same stress ratio, the cracks propagated faster in the BM and the HAZ and slower in the WM. An equation for the steady-state FCG rate was obtained.
- (3) Based on the observations of the crack paths in the different regions of the sample, the fatigue crack in the BM of the welded joint propagated intergranularly or transgranularly according to the orientation of the pearlite lamella and the driving force of the crack tip. The FCP paths in the WM were relatively tortuous due to the effects of equiaxed austenite and multipass welding. The FCP in the HAZ specimens had two forms. For the HAZ specimens where the crack growth rate was slightly lower than that in the BM, the results showed that the fatigue crack propagated in the fine-grained region of the HAZ. For the HAZ specimen where the crack propagated across the WM and the FL, the EBSD results showed that the fatigue crack propagated tortuously into the HAZ along the high-angle Type II and Type I boundaries in the WM.
- (4) The fracture morphology of the BM was basically the same as that of the HAZ, which contained a large number of fatigue steps and secondary cracks, and

there were no fatigue striations. For the WM, the initial stage of fatigue crack growth had quasi-cleavage characteristics such as rivers and tearing edges. In the middle stage, a large number of fatigue striations appeared. The stage of instability propagation exhibited a single dimple-type ductile fracture characteristic.

References

- Li L Y, Xiao J, Han B, and Wang X L, *Int J Pres Ves Pip* **179** (2020) 104026.
- Zhang L J, Pei Q, and Zhang J X, *Mater Des* **64** (2014) 462.
- Qian X D, Wang Y, Richard Liew J Y, and Zhang M H, *Eng Struct* **92** (2015) 84.
- Wang H T, Wang G Z, Xuan F Z, and Tu S T, *Eng Failure Anal* **28** (2013) 134.
- Thurston K V S, Gludovatz B, Yu Q, Laplanche G, George E P, and Ritchie R O, *J Alloys Compd* **794** (2019) 525.
- Kacar R, and Acarer M, *J Mater Process Technol* **152** (2004) 91.
- Liu H B, Yang S L, Xie C J, Zhang Q, and Cao Y M, *J Alloys Compd* **741** (2018) 188.
- Karolczuk A, Kowalski M, Bański R, and Żok F, *Int J Fatigue* **48** (2013) 101.
- Shang Y B, Shi H J, Wang Z X, and Zhang G D, *Mater Des* **88** (2015) 598.
- Giorgetti V, Santos E A, Marcomini J B, and Sordi V L, *Int J Pres Ves Pip* **169** (2019) 223.
- Kunnathur P Y, Perumal A. V, and Rajasekaran D, *Trans Indian Inst Met* **71** (2018) 2575.
- Ming H, Zhang Z, Wang J, and Han E H, *Mater Charact* **148** (2019) 100.
- Hou J, Peng Q J, Takeda Y, Kuniya J, Shoji T, and Wang J Q, *J Mater Sci* **45** (2010) 5332.
- Öztoprak N, Yeni Ç E, and Kiral B G, *Trans Indian Inst Met* **72**(2) (2019) 511.
- Vidyarthi R S, Kulkarni A, and Dwivedi D K, *Mater Sci Eng A* **695** (2017) 249.
- Brayshaw W J, Cooper A J, and Sherry A H, *Eng Failure Anal* **97** (2019) 820.
- Yang J, and Wang L, *Eng Fract Mech* **192** (2018) 12.
- Fan K, Wang G Z, Xuan F Z, and Tu S T, *Eng Fract Mech* **136** (2015) 279.
- Blouin A, Chapuliot S, Marie S, Niclaeys C, and Bergheau J. M, *Eng Fract Mech* **131** (2014) 58.
- Thirugnanam A, Sukumaran K, Raghukandan K, Pillai U T S, and Pai B C, *Trans Indian Inst Met* **58** (2005) 777.
- Yang J, Wang G Z, Xuan F Z, Tu S T, and Liu C J, *Mater Des* **55** (2014) 542.
- Xie Y, Wu Y Q, Burns J, and Zhang J S, *Mater Charact* **112** (2016) 87.
- Rathod D W, Pandey S, Singh P K, and Kumar S, *J Nucl Mater* **493** (2017) 412.
- Ghassen B S, Stéphane C, Arnaud B, Philippe B, and Clémentine J, *Procedia Struct Integr* **13** (2018) 619.
- Wang X F, Shao C D, Liu X, and Lu F G, *J Mater Sci Technol* **34** (2018) 720.
- Du L Y, Wang G Z, Xuan F Z, and Tu S T, *Nucl Eng Des* **265** (2013) 145.
- Velu M., *Mater Today Proc* **5**(5) (2018) 11364.
- Kangazian J, and Shamanian M, *Mater Charact* **155** (2019) 109802.
- Dong L J, Peng Q J, Han E H, Ke W, and Wang L, *J Mater Sci Technol* **34**(8) (2018) 1281.
- Zhu R L, Wang J Q, Zhang Z M, and Han E H, *Corros Sci* **120** (2017) 219.
- Zhu R L, Wang J Q, Zhang L T, Zhang Z M, and Han E H, *Corros Sci* **112** (2016) 373.
- Dong L J, Peng Q J, Xue H, Han E H, Ke W, and Wang L, *Corros Sci* **132** (2018) 9.
- Huang J Y, Chiang M F, Jeng S L, Huang J S, and Kuo R C, *J Nucl Mater* **432** (2013) 189.
- Yeh T K, Huang G R, Wang M Y, and Tsai C H, *Prog Nucl Energ* **63** (2013) 7.
- Cortés R, Rodríguez N K, Ambriz R R, López V H, Ruiz A, and Jaramillo D, *Mater Sci Eng A* **745** (2019) 20.
- Wang B, Lei B B, Wang W, Xu M, and Wang L, *Eng Failure Anal* **58** (2015) 56.
- Jang C, Cho P Y, Kim M, Oh S J, and Yang J S, *Mater Des* **31** (2010) 1862.
- Wang W, Liu T G, Cao X Y, Lu Y H, and Shoji T, *Mater Sci Eng A* **729** (2018) 331.
- Ki H, Kim C.S, Jeon Y.C, and Kwun S I, *Mater. Sci. Forum* **580-582** (2008) 593.
- Huang J Y, Young M C, Jeng S L, Yeh J J, Huang J S, and Kuo R C, *Mater Trans* **49** (2008) 1667.
- Nelson T W, Lippold J C, and Mills M J. *Sci Technol Weld Joi* **3**(5) (2013) 249.
- Wang C X, Wang T, Cao L L, and Zhang G J, *J Alloys Compd* **790** (2019) 563.
- Hou J, Peng Q J, Lu Z P, Shoji T, Wang J Q, Han E H, and Ke W, *Corros Sci* **53** (2011) 1137.
- Hou J, Peng Q J, Takeda Y, Kuniya J, and Shoji T, *Corros Sci* **52** (2010) 3949.
- Sarikka T, Ahonen M, Mougnot R, Nevasmaa P, Karjalainen-Roikonen P, Ehrnsten U, and Hänninen H, *Int J Pres Ves Pip* **145** (2016) 13.
- Hong H L, Zhu R L, Zhang Z M, Wang J Q, Han E H, Ke W, and Su M X, *Mater Sci Eng A* **669** (2016) 279.
- Shenoy M M, Kumar R S, and McDowell D L, *Int J Fatigue* **27** (2005) 113.
- Smith R A, *Int J Fracture* **9**(3) (1973) 352.
- Yanagimotoa F, Hemmi T, Suzuki Y, Takashim Y, Kawabata T, and Shibamura K, *Acta Mater* **177** (2019) 96.
- Guan M F, and Yu H. *Sci China Technol Sci* **56** (2013) 71.
- Wert J A, and Huang X, *Philos Mag* **83** (2003) 969.
- Winther G, *Acta Mater* **51** (2003) 417.
- Hu D Y, and Wang R Q, *Mater Sci Eng A* **515** (2009) 183.
- Xiao X P, Yi Z Y, Chen T T, Liu R Q, and Wang H, *J Alloys Compd* **660** (2016) 178.
- Goldsmith N T, Wanhill R J H, and Molent L, *Eng Failure Anal* **96** (2019) 426.
- Ivanova V S, Kunavin S A, and Shanjavskij A A, *Proceedings of The 7th International Conference On Fracture (ICF7)*, Pergamon, Oxford (1989), p 3677.

Publisher's Note Springer Nature remains neutral with regard to jurisdictional claims in published maps and institutional affiliations.